Materials Characterization 195 (2023) 112494

Contents lists available at ScienceDirect

Materials Characterization

journal homepage: www.elsevier.com/locate/matchar

Enhanced mechanical properties and high electrical conductivity of copper alloy via dual-nanoprecipitation

Meng Zhou [a,c,d,*], Yongfeng Geng [a,b], Yi Zhang [a,c,d,*], Yijie Ban [a], Xu Li [e], Yanlin Jia [f], Shengli Liang [a], Baohong Tian [a,c,d], Yong Liu [a,c,d], Alex A. Volinsky [g]

[a] School of Materials Science and Engineering, Henan University of Science and Technology, Luoyang 471023, PR China
[b] State Key Laboratory of Metal Matrix Composites, Shanghai Jiao Tong University, Shanghai 200240, China
[c] Provincial and Ministerial Co-construction of Collaborative Innovation Center for Non-ferrous Metal new Materials and Advanced Processing Technology, Henan Province, Luoyang 471023, PR China
[d] Henan Province Key Laboratory of Nonferrous Materials Science and Processing Technology, Luoyang 471023, PR China
[e] Center for Advanced Measurement Science, National Institute of Metrology, Beijing 100029, PR China
[f] College of Materials Science and Engineering, Central South University, Changsha, 410083, China
[g] Department of Mechanical Engineering, University of South Florida, Tampa 33620, USA

ARTICLE INFO

Keywords:
Cu-Co-Si-Ti-Ce alloy
Precipitation
Multiple strengthening
Mechanical properties

ABSTRACT

Copper alloys are widely used as lead frames, electric contact wires and pantographs due to their high electrical conductivity and excellent mechanical properties. At present work, a medium electrical conductivity and excellent mechanical properties of Cu-Co-Si-Ti-Ce alloy was obtained by the vacuum melting process with the optimum performance of 225 HV, 702.5 MPa and 40.8% IACS aging at 500 °C for 60 min via the combinations of multiple strengthening. It can be inferred that the high-volume fraction of Goss, Brass, copper and S texture was one of the main reasons for the increase of micro-hardness by comparing the texture content at different conditions. Moreover, it was observed that Co_2Si and $Co_{16}Ti_6Si_7$ phases exhibited coherent and semi-coherent interface relationships with the copper matrix, respectively, which can relieve the interfacial stress and reduce the interface energy by GPA analysis. Finally, the contributions of solid solution strengthening, work-hardening, grain boundary strengthening and precipitation strengthening were calculated, contributing most to the precipitation strengthening.

1. Introduction

Copper alloys have been widely used in the electronic and electrical industries, lead frames, aerospace and other fields due to the combination of high strength and high electrical conductivity, which can be attributed to the precipitation of nanoscale particles during aging [1–5]. Up to now, Cu-Ni-Si alloy [6,7], Cu-Ni-Sn alloy [8,9], Cu-Fe-P alloy [10], Cu-Cr-Zr alloy [11,12], Cu—Ti alloy [13,14] and et al. can be potential replacements for the Cu—Be alloys, as a result of toxicity for beryllium was found to be harmful to human health especially in the manufacturing process [15]. Especially, Cu-Ni-Si systems alloys have attracted much interest due to their high strength and good electrical conductivity [16–18]. The low content of Ni and Si make Cu-Ni-Si alloys used as lead frames due to the combination of high strength and good electrical conductivity. The high content of Ni and Si make Cu-Ni-Si alloys higher strength, which are potential elastic conductive materials [4,17,18].

Higher strength and better conductivity of copper alloys are required for the rapid development of equipment and technologies. One of the most effective ways is to add trace alloy elements, accompanied by refining the grains, promoting precipitation and finally strengthening the matrix. Advantageous addition elements include Co [5,19], Ti [13,14], Cr [20,21], Al [17,22], Mg [23], et al. Zhao et al. [24] investigated the microstructure and properties of a Cu-Ni-Si-Co-Cr alloy with high strength and high conductivity. It can be inferred that Co addition promoted the precipitation of Cr, Ni and Si solute elements from the matrix, while inhibited the growth of the $(Cr, Co)_2Si$, resulting in high strength and good electrical conductivity of studied alloy. Cheng et al. [25] observed the existence of three kinds of nanoscale precipitates, ordered face-centered cubic δ-Ni_3Si, orthorhombic δ-Ni_2Si and ordered

* Corresponding authors.
E-mail addresses: zhoumeng0902@126.com (M. Zhou), yizhang@haust.edu.cn (Y. Zhang).

https://doi.org/10.1016/j.matchar.2022.112494
Received 28 August 2022; Received in revised form 3 November 2022; Accepted 15 November 2022
Available online 17 November 2022

face-centered cubic (Ni, Cr, Si)-rich phase, increasing the mechanical properties. Lei et al. [22] observed that Al addition enhanced the anti-stress relaxation property and strength by refining grain size and promoting the precipitation during the aging process. The other method is to optimize the thermo-mechanical treatment following by an aging process. Apart from alloying, the different aging parameters and related morphology of the precipitated phases at different stages of the heat treatment process play a vital role in the mechanical performance of copper alloys. The thermomechanical treatment can result in a fine structure and supersaturated solid solution. By following this with an aging process, mainly including cold rolling and aging treatment, the copper alloys are subsequently strengthened due to the multiple strengthening mechanisms, which are employed commercially on a wide variety of nonferrous materials, especially in some age-harden able aluminum alloys with great success [18,22]. Additionally, the precipitation purifies the Cu matrix to guarantee electrical conductivity. Therefore, adding trace alloying elements, understanding and optimization of the aging process to control the precipitation process are the vital key to improve the overall property of copper alloys.

In our previous work, the effects of Ti and Ce addition on hot deformation were carried out on the Gleeble-1500 simulator in order to understand the hot deformation studies [26,27]. To understand the optimum aging parameters and age-hardening mechanisms in Cu-Co-Si-Ti-Ce alloy, it is essential to investigate the microstructure evolution and effects on the mechanical properties during aging treatment. Currently, the microstructure evolution and mechanical properties of Cu-Co-Si-Ti-Ce alloy were investigated by the scanning electron microscope (SEM), electron backscatter diffraction (EBSD), transmission electron microscope (TEM) and high-resolution transmission electron microscope (HRTEM) during the aging process. In addition, the details of the interfacial relationship between precipitates and Cu matrix can effectively affect the stress state and accordingly the strength of the alloy. The strain field distribution can be evaluated through the geometric phase analysis (GPA) of HRTEM images.

2. Materials and methods

2.1. Materials preparation

The prepared raw materials mainly including electrolytic cathode copper, pure Co, Si, Cu-45%Ti and Cu-19%Ce, were cut into small pieces to facilitate the ingredients and melting. The melting of alloys was carried out in a medium frequency vacuum induction furnace (ZG-0.01-40-4), and a certain amount of argon was required to be put in at the same time to prevent the oxidation of alloys. The nominal composition and actual composition of the alloy designed can be observed in Ref. [26 and 27]. In order to remove the casting defects of the ingot, the risers of the ingots cooled to room temperature were cut off, and the surface oxide scale of the remaining ingots was removed. Then the Cu-Co-Si-Ti-Ce alloy ingot was annealed at 960 °C × 1 h by a vacuum heat treatment furnace, following by extruded into a bar with a diameter of 30 mm by the XJ-500 hot extrusion machine. The hot extruded bar was heated at 960 °C × 1 h in the vacuum heat treatment furnace and water cooling, making the solute atoms Co, Si, Ti and Ce enter into the matrix to form a supersaturated solid solution. The solution- treated samples were cut into specimens with the size of 100 mm × 10 mm × 1 mm by wire cutting, and then 50% cold rolling (each reduction is 5% of the thickness). Finally, aging treatment at a different time (10–480 min) and temperature (400–550 °C) were carried out in the vacuum tubular furnace. The performance tests mainly include electrical conductivity by ZY9987 digital micro-ohm meter, micro-hardness by HVS-1000 hardness tester and the tensile strength tests by the AG-I 250 KN machine with a speed of 5.0 mm/min at room temperature.

2.2. Characterizations

The microstructure evolution during the aging process was observed by SEM, EBSD, TEM and HRTEM. The JSM-7800F backscatter scanning electron microscope with an EBSD probe was used to observe the tensile fractures and EBSD tests. The samples were mechanically polished to remove the rough scratches, followed by the electro-polishing for 1 min with DC power supply and magnetic stirrer in a solution of 50% CH_3CH_2OH and 50% H_3PO_4 at a voltage of 5 V at 25 °C. The TEM observation was carried out on the FEI Talos F200X transmission electron microscope, and the sample was prepared by mechanical polishing to a thickness of about 50 μm and then thinned by Gatan 695 ion thinner. First, the samples are thinned to the appearance of holes under the condition of ion beam energy of 5 kev and ion gun angle of ±8°. Subsequently, the samples can be used for TEM observations after being thinned for 5 min at 4.5 kev ± 6°, 5 min at 4 kev ± 4° and 5 min at 3 kev ± 3°, respectively.

3. Results

3.1. Conductivity and mechanical properties

Fig. 1 shows the micro-hardness and electrical conductivity of Cu-Co-Si-Ti-Ce alloy aging at different temperatures and times, with approximate boundaries between different aging stages indicated. It can be seen that there are three main stages in the aging process, including under aging stage, peak aging stage and over aging stage [24,28]. In the under aging stage, due to the strong supersaturation of copper alloy in the early aging stage, the precipitation force and precipitation rate of the second phase are large, resulting in a rapid increase in the microhardness and electrical conductivity. Subsequently, the microhardness reaches the maximum value, corresponding to the peak aging stage, which can be attribute to the maximum value of precipitation rate in this stage. With the further extension of aging time, the micro hardness starts to decrease after reaching the over aging stage, which can be attributed to the growth and softening of precipitates caused by the release of lattice distortion energy. In addition, precipitation is a diffusion process of atoms. With the increase of aging temperature, atomic activity increases and precipitation is promoted, resulting in higher microhardness of alloy. However, because of the softening effect caused by the growth of precipitates and the release of lattice distortion energy in the over-aging stage with aging temperature exceeds a certain limit, the microhardness begin decrease.

In order to investigate the dependencies of the micro-hardness and electrical conductivity of Cu-Co-Si-Ti-Ce alloy under the peak-aging stage, the micro-hardness and electrical conductivity of Cu-Co-Si-Ti-Ce alloy under different aging conditions were shown in Fig. 2(A) and (B). The curves for micro-hardness illustrated that the micro-hardness increased in the under-aging stage and then decreased in the over-aging stage. With the aging time from 0 (cold rolling state) to 60 min, the micro-hardness of Cu-Co-Si-Ti-Ce alloy increased rapidly and reached the peak value of 225 HV at 500 °C for 60 min, 23% higher than cold rolling state (173.9 HV). With the aging time exceeding 60 min, the micro-hardness decreased gradually, while it was still higher than that of the cold rolling state (185.5 HV, almost 6.5% higher) due to the aging strengthening. In addition, with the aging temperature exceeding 500 °C, the micro-hardness also showed a downward trend (from 225 HV to 207.7 HV), as illustrated in Fig. 2(B). Referring to Fig. 2(A) and (B), the electrical conductivity of Cu-Co-Si-Ti-Ce alloy increased sharply and then grew slowly with prolonged aging time and increased of temperature. For example, the aging time from 0 min (cold rolling state) to 480 min, and the aging temperature increase from 400 °C to 550 °C, the electrical conductivity increases from 21.3% IACS to 46.5 %IACS and from 37.8 %IACS to 43.7 %IACS, respectively.

Moreover, Fig. 2(A) and (B) also manifested the tensile fractures under specially selected conditions, and the magnified images of

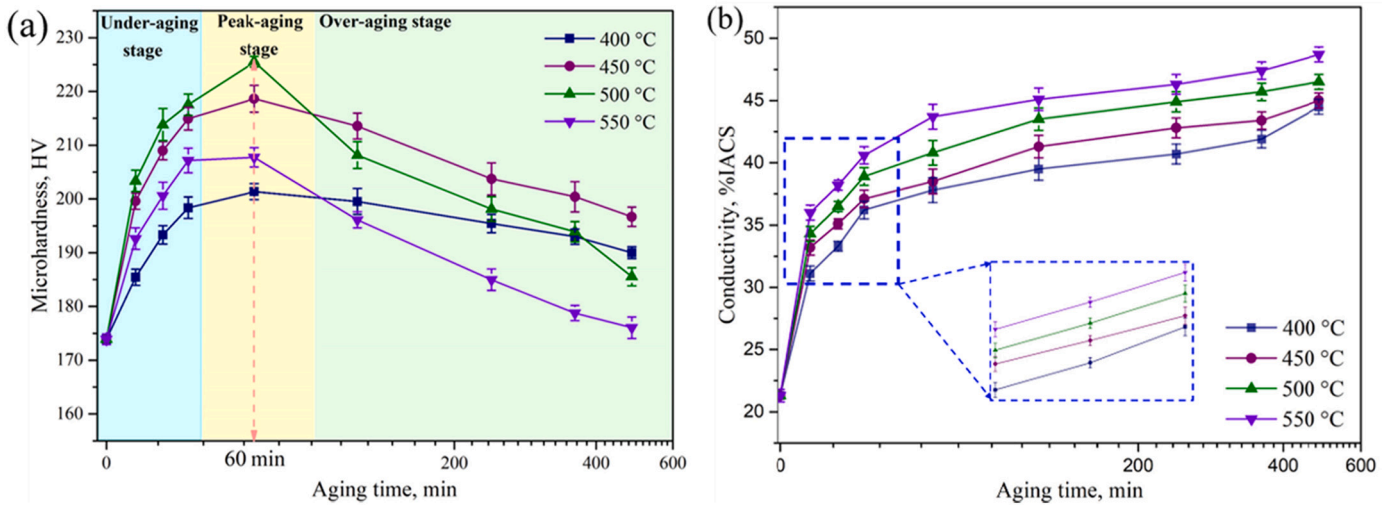

Fig. 1. Micro-hardness and electrical conductivity of Cu-Co-Si-Ti-Ce alloy aging at different temperatures and time: (a) micro-hardness, (b) electrical conductivity.

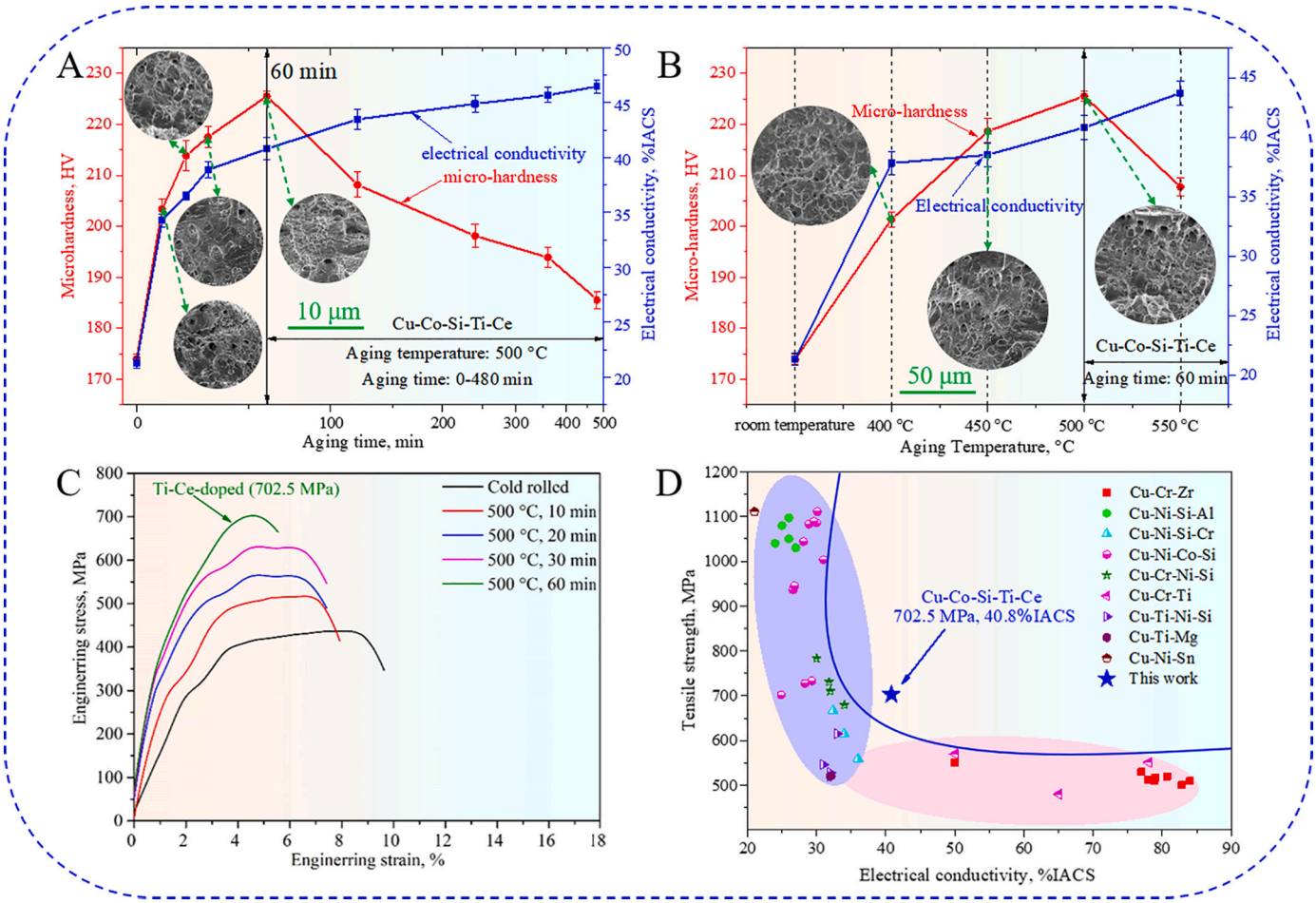

Fig. 2. Mechanical properties and electrical conductivity of Cu-Co-Si-Ti-Ce alloy: (A) Variation of micro-hardness and electrical conductivity with aging time for Cu-Co-Si-Ti-Ce alloy aged at 500 °C, (B) Variation of micro-hardness and electrical conductivity with aging temperature for Cu-Co-Si-Ti-Ce alloy aged at 60 min, (C) tensile strength of Cu-Co-Si-Ti-Ce alloy under different conditions, (D) comparison of tensile strength vs. electrical conductivity between the present Cu-Co-Si-Ti-Ce alloy and conventional copper alloys [11,12,17,19,22,25,32–37].

corresponding tissues can be observed in the supplementary materials (Fig. S5). Generally speaking, the number and size of dimples are important indexes to evaluate the plasticity of metals, which mainly includes average diameter and depth [28–31]. In other words, the larger the dimple size, the better the plasticity of the material under the same fracture conditions. With the aging time from 10 min to 60 min (Fig. 2 (A)), the micro-hardness of Cu-Co-Si-Ti-Ce alloy increased rapidly, accompanied by the decrease of the number and size of dimples. The

same phenomenon can be also observed in Fig. 2(B). With the aging temperature exceeding 500 °C, the number and size of dimples increased gradually, implying the increase of plasticity.

Corresponding tensile curves aging at 500 °C for a different time were illustrated in Fig. 2(C). It can be observed that highest tensile strength (702.5 MPa) can be obtained by aging at 500 °C for 60 min. Finally, the optimum aging parameter was aging at 500 °C for 60 min, accompanied by the excellent aging performance of 225 HV, 702.5 MPa and 40.8% IACS. The comparison of tensile strength vs. electrical conductivity between the present Cu-Co-Si-Ti-Ce alloy and conventional copper alloys can be obtained in Fig. 2(D) [11,12,17,19,22,25,32–37], and it can be observed that Cu-Co-Si-Ti-Ce alloy possessed good comprehensive mechanical properties.

3.2. EBSD analysis

Fig. 3 shows the EBSD maps of Cu-Co-Si-Ti-Ce alloy aging at 500 °C for 60 min and 120 min, respectively. As illustrated in Fig. 3(A-C) for the IPF map, KAM map and All Euler map, it can be observed that there were still some typical deformed grains, although aging for 60 min. Moreover, the grains in microstructure showed different orientations with three different Euler angles (φ_1, Φ, φ_2), such as (115.5, 47.1, 23.8), (4.0, 45.1, 76.3) and (273.0, 38.3, 51.0). With prolong aging time to 120 min, some fine recrystallized grains appeared due to the dynamic recovery and dynamic recrystallization, resulting in the orientation randomization. In addition, it can be seen that the internal stress of the samples after 120 min aging treatment decreased through the KAM map, indicating the weakening of work hardening. Meanwhile, the grains in the samples aging for 120 min showed more different orientations, such as (337.8, 43.9, 23.8), (324.2, 44.6, 26.4), (179.4, 44.2, 77.1), (175.3, 33.2, 79.1) and (99.7, 22.4, 51.3). According to the KAM maps (Fig. 3(B) and (E)) and corresponding data (Fig. 3(G)), the geometric necessary dislocation (GND) density of Cu-Co-Si-Ti-Ce alloy aging for 60 min and 120 min can be calculated by referring to Ref. 38 and 39. Therefore, the GND density for two different samples can be calculated to be $\rho = 2\theta/\mu b = 2.5 \times 10^{14}/m^2$ and $\rho = 2\theta/\mu b = 1.8 \times 10^{14}/m^2$, respectively, 28% lower than aging for 60 min.

It is worth noting that the samples aging for 60 min possessed more obvious orientation compared with aging for 120 min. Consequently, it is necessary to investigate the orientation (mainly including texture evolution) of the Cu-Co-Si-Ti-Ce alloy after aging for a different time. Fig. 3(H) and (I) show the ⟨100⟩, ⟨110⟩, ⟨111⟩ pole figures and 3D-ODF maps of Cu-Co-Si-Ti-Ce alloy aging for 60 min and 120 min, respectively. On the one hand, it presented a strong texture after aging for 60 min with an average intensity of 10.5 mud, almost twice as much as 120 min. On the other hand, the distributions of texture components showed big differences according to the <100>, <110> and ⟨111⟩ pole figures tilted away from Normal Direction (ND), which was given in Fig. 3(G). It can be seen that distributions of texture components for <100>, <110> and < 111> pole figures aging for 60 min were extremely uneven, especially in the range of 0–10°of <110> pole figure. Instead, the distributions of texture components were more uniform after aging for 120 min. This indicated that both texture position and texture intensity were changed by the dynamic recovery and dynamic recrystallization, which were consistent with the results of EBSD maps in Fig. 3(A-F). Furthermore, the texture components for the Cu-Co-Si-Ti-Ce alloy after different aging time were calculated by texture component maps in Fig. S1 and the corresponding contents of texture were illustrated in Fig. 3(K). For example, it can be seen that the volume fraction of main texture components for Goss, Brass, copper and S texture after 60 min aging process were 22.7%, 46.8%, 32.6% and 46%, respectively. While the volume fraction of Goss, Brass, copper and S texture decreased to 7.48%, 12.6%, 5.24% and 7.08% with prolonged aging time to 120 min. In this aging time range, the volume fraction of main texture components decreased,

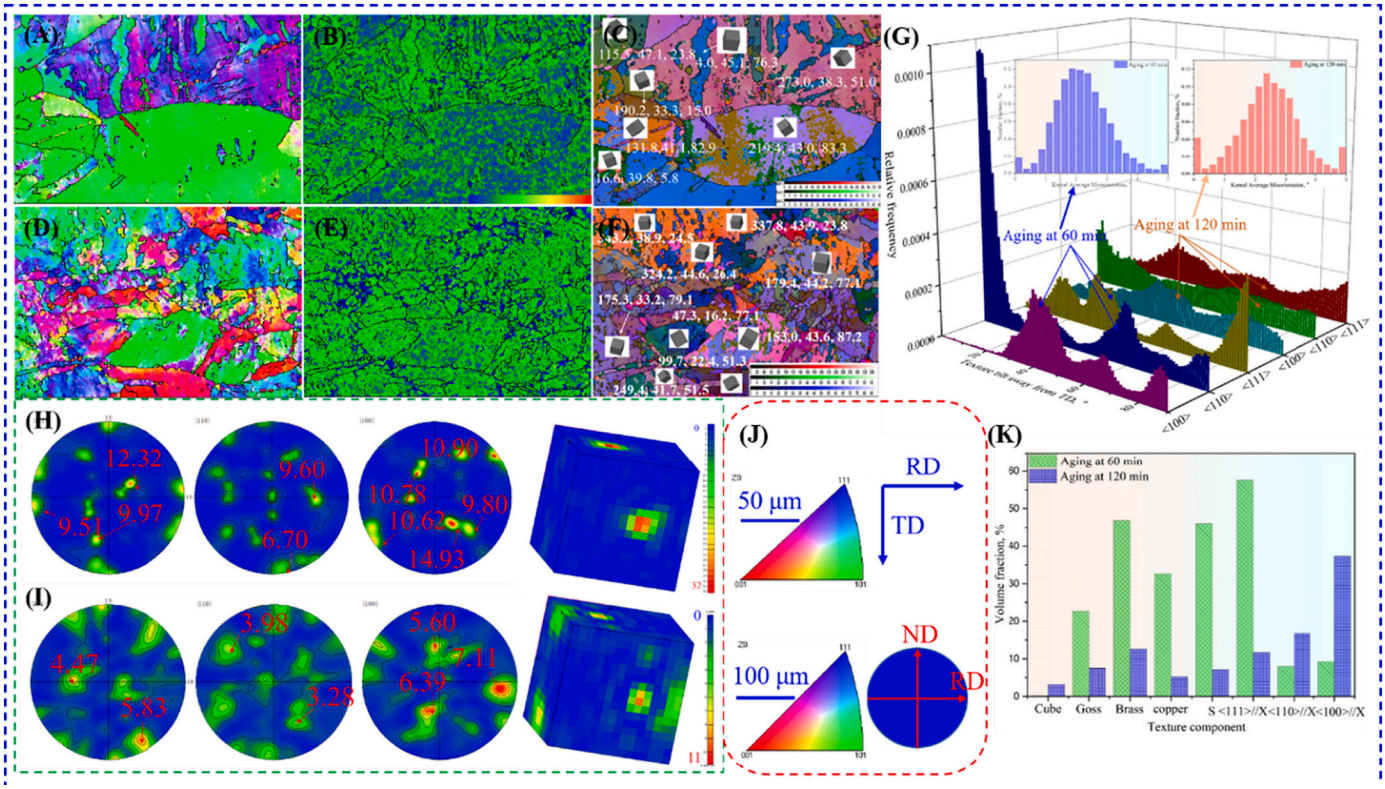

Fig. 3. EBSD maps of Cu-Co-Si-Ti-Ce alloy aging at 500 °C for different time: (A-C) IPF map, KAM map and All Euler map aging for 60 min, respectively. (D—F) IPF map, KAM map and All Euler map aging for 120 min, respectively. (G) <100>, <110> and < 111> pole figures tilted away from Normal Direction (ND) and the data for KAM map, (H) pole figures and 3D-ODF map aging for 60 min, (I) pole figures and 3D-ODF map aging for 120 min, (J) figure legends for EBSD maps, (K) texture components aging at 500 °C for 60 min and 120 min.

whereas the fraction of randomly oriented grains increased, indicating a slight texture weakening. Simultaneously, as shown in Fig. 4, representing the Grain Boundary (GB) maps and Misorientation angle distribution of Cu-Co-Si-Ti-Ce alloy aging at 500 °C for 60 min and 120 min, respectively, the distribution of misorientation angles was almost consistent, showing a considerable concentration at the low misorientation angles, namely low angle grain boundaries (LAGBs, misorientation angle<15°), where it can be seen that the percent of high angle grain boundaries (HAGBs) was 13.1% for the sample under 60 min aging process. And the percent of HAGBs increased to 15.4% after 120 min aging.

3.3. TEM analysis

Fig. 5 shows the HRTEM images, corresponding Fast Fourier Transform (FFT) patterns and GPA analysis of the Cu-Co-Si-Ti-Ce alloy aging at 500 °C for 60 min. The morphology of precipitates was shown in Fig. 5 (a), (c), (g) and (k), respectively, taken from $[001]_{Cu}$ direction. And corresponding FFT patterns of HRTEM images were illustrated in Fig. 5 (b), (h) and (l), respectively. The precipitate (Fig. 5(a)) can be determined to be Co_2Si with the orthorhombic system of a = 7.109, b = 4.918 and c = 3.737 (Fig. 6(a)), as evidenced by the super-lattice spots of the Co_2Si phase (Fig. S4(c)). Similarly, the precipitate in Fig. 5(c) can be also determined to be Co_2Si phase, indicating the rod shape of Co_2Si phase with a large diameter-thickness ratio. The precipitate in Fig. 5(g) and (k) can be both determined to be $Co_{16}Ti_6Si_7$ phase with the cubic system of a = b = c = 11.202 (Fig. 6(b)), as evidenced by the super-lattice spots of the $Co_{16}Ti_6Si_7$ phase (Fig. 6(d) and (e)), indicating that the $Co_{16}Ti_6Si_7$ phase possessing a disk-like shape. To verify the correctness of calibrated phases, we simulated the phase structure of Co_2Si and $Co_{16}Ti_6Si_7$ and spots of Co_2Si phase with $[2\bar{3}0]$ zone axis, $Co_{16}Ti_6Si_7$ phase with [001] zone axis and $Co_{16}Ti_6Si_7$ phase with $[5\bar{1}\bar{5}6]$ zone axis. The results of the above simulations (Fig. 6) can be well-matched with the actual spots (Fig. 5(b), (h) and (l)), which proved the accuracy of the results. Moreover, the enlarged part of the green rectangle in Fig. 5(a), the enlarged part of green rectangle in Fig. 5(k) and the enlarged part of blue and yellow rectangles in Fig. 3(g) were illustrated in Fig. S2(a-c), respectively, where can observe the atomic arrangement of precipitates clearly.

The FFT pattern results in Fig. 5(b) showed that there were obvious orientation relationship (OR) between the Co_2Si phase and copper matrix, which can be expressed as $(020)_{Cu} \parallel (320)_{Co2Si}$, $(200)_{Cu} \parallel (002)_{Co2Si}$, $(220)_{Cu} \parallel (322)_{Co2Si}$ and $[001]_{Cu} \parallel [2\bar{3}0]_{Co2Si}$. However, it can be observed that the Co_2Si phase was not completely coherent with the matrix, indicating that there was a certain lattice mismatch between them. Lattice mismatch induced by the formation and growth of Co_2Si phase produced extra stains at the interface between Co_2Si phase and copper matrix, which can be evaluated by the geometric phase analysis (GPA) of HRTEM images [40]. As illustrated in Fig. 5(d-f) for the GPA maps, the color scale indicated the strain changes, positive values representing the tensile strains and negative values representing the compressive strains, where showed the strain distributions around the Co_2Si in the specimen calculated by GPA for (002), (320) and (322) planes, respectively. It can be observed that there was a little bit of strain distribution in the (002), (320) and (322) planes of the Co_2Si phase, although the strain values along different directions were different. By filtering the HRTEM images of the Co_2Si phase Fig. S3(a), we obtained the Inversed FFT images of (002), (320) and (322) planes Fig. S3(c-e), in which many interface defects, such as periodic interface dislocations were observed. These

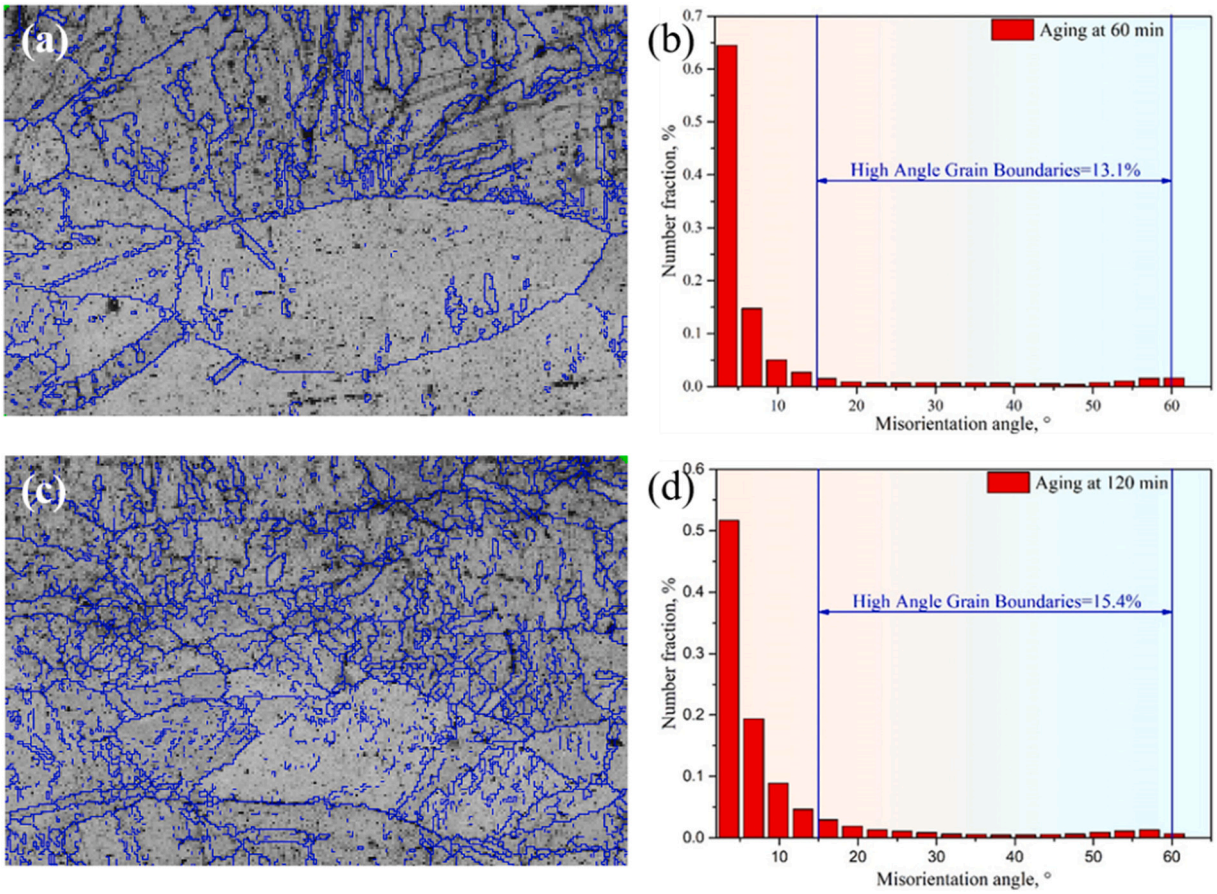

Fig. 4. Grain Boundary (GB) maps and Misorientation angle distribution of Cu-Co-Si-Ti-Ce alloy aging at 500 °C for 60 min and 120 min: (a) (b) 60 min, (c) (d) 120 min.

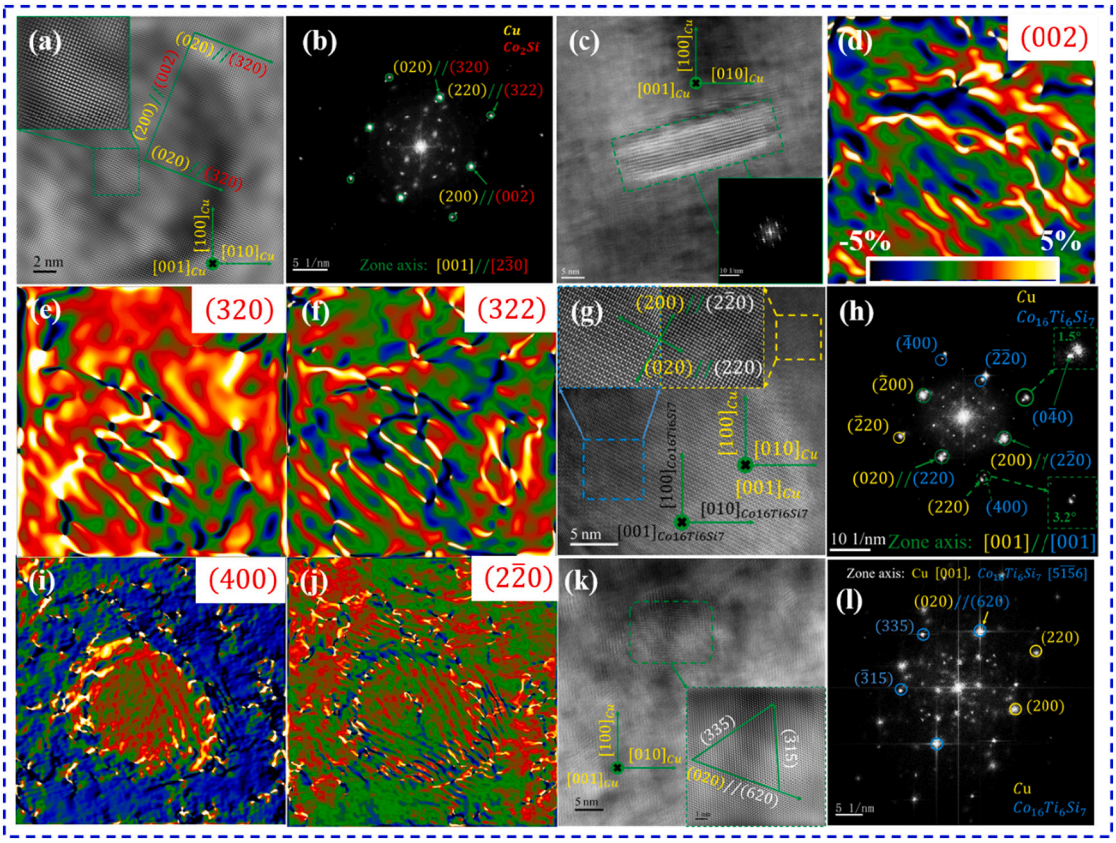

Fig. 5. HRTEM images, corresponding FFT patterns and GPA analysis of the Cu-Co-Si-Ti-Ce alloy aging at 500 °C for 60 min: (a) (c) HRTEM image taking from $[001]_{Cu}$ direction, (b) FFT pattern of (a), (d) (e) (f) The strain distributions around the Co_2Si in the specimen calculated by GPA for (002), (320) and (322) planes, respectively, (g) HRTEM image taking from $[001]_{Cu}$ direction, (h) FFT pattern of (g), (i) (j) The strain distributions around the $Co_{16}Ti_6Si_7$ in the specimen calculated by GPA for (400) and $(2\bar{2}0)$ planes, respectively, (k) HRTEM image taking from $[001]_{Cu}$ direction, (l) FFT pattern of (k).

interfacial structural ledges and dislocations between the Co_2Si phase and copper matrix can relieve interfacial stress and reduce the interface energy [29].

The OR between $Co_{16}Ti_6Si_7$ phase and copper matrix was different from that Co_2Si, as illustrated in Fig. 5(g-l), which can be expressed as $(020)_{Cu} \parallel (220)_{Co16Ti6Si7}$, $(200)_{Cu} \parallel (2\bar{2}0)_{Co16Ti6Si7}$, $[001]_{Cu} \parallel [001]_{Co16Ti6Si7}$, $(220)_{Cu} \nparallel (400)_{Co16Ti6Si7}$ and $(2\bar{2}0)_{Cu} \nparallel (0\bar{4}0)_{Co16Ti6Si7}$. The above results proved that the Co_2Si phase was semi-coherent with the copper matrix. In other words, $(220)_{Cu}$ and $(400)_{Co16Ti6Si7}$, $(2\bar{2}0)_{Cu}$ and $(0\bar{4}0)_{Co16Ti6Si7}$ were not parallel instead of angle deviation of 3.2° and 1.5°, respectively. It was worth mentioning that the angle deviation between $(220)_{Cu}$ and $(400)_{Co16Ti6Si7}$ was almost twice of $(2\bar{2}0)_{Cu}$ and $(0\bar{4}0)_{Co16Ti6Si7}$. The semi-coherent relationship between the $Co_{16}Ti_6Si_7$ phase and copper matrix will inevitably cause the internal strain, which can be also evaluated by the GPA analysis of HRTEM images. Fig. 5(i) and (j) showed the strain distributions around the $Co_{16}Ti_6Si_7$ in the specimen calculated by GPA for (400) and $(2\bar{2}0)$ planes, respectively. It can be observed that the strain gradient was near zero with the interface relationship of $(200)_{Cu} \parallel (2\bar{2}0)_{Co16Ti6Si7}$. However, there was a large strain gradient and a large strain field in $(220)_{Cu} \nparallel (400)_{Co16Ti6Si7}$, in which can observe large compressive strain in the copper matrix and relatively large tensile strain at the interface of $Co_{16}Ti_6Si_7$ phase and copper matrix, but no obvious strain in the $Co_{16}Ti_6Si_7$ phase. By filtering the HRTEM images of the $Co_{16}Ti_6Si_7$ phase Fig. S4(a), the IFFT images of (400) and $(2\bar{2}0)$ planes were obtained. As illustrated in Fig. S4(c), there was no lattice distortion observed in the precipitate, indicating no obvious strain field. Only a few dislocations at the interface between the $Co_{16}Ti_6Si_7$ phase and copper matrix were observed. In the IFFT image of $(400)_{Co16Ti6Si7}$, a large number of dislocations were distributed on the interface and copper matrix marked by white oval, consisting with the GPA analysis in Fig. 5.

4. Discussion

4.1. Effects of aging on electrical conductivity and mechanical properties

It is well known that the factors of electrical conductivity mainly include the effects of electrons scattering by defects such as grain boundaries, dislocations, solid solution atoms and et al. [17,18,24]. The mechanical properties are mainly affected by the interactions between precipitates and dislocations [40,41]. As shown in Figs. 1 and 2, the electrical conductivity and micro-hardness of the Cu-Co-Si-Ti-Ce alloy changed significantly with the aging process, both higher than those of the solid solution state. In the early stage of aging, both electrical conductivity and micro-hardness increased rapidly due to the precipitation of the Co_2Si and $Co_{16}Ti_6Si_7$phases. Then, the peak aging stage was reached in the subsequent aging process, reaching the maximum value for the micro-hardness. The micro-hardness began to decrease with exceeding the peak aging stage, which can be attributed to the obvious growth of precipitates, significant enhancement of dynamic recovery and dynamic recrystallization [42,43]. As given in Fig. 3(D), some fine recrystallized grains have appeared due to the dynamic recovery and dynamic recrystallization, resulting in the decrease of micro-hardness (Fig. 1(a) and Fig. 2(A)). Moreover, when the aging temperature exceeded 500 °C, the micro-hardness also decreased due to the growth of precipitates and the enhancement of the dynamic softening effect (Fig. 1 (a) and Fig. 2(B)). In the aspect of electrical conductivity, the change of electrical conductivity is closely related to the number of solute atoms in

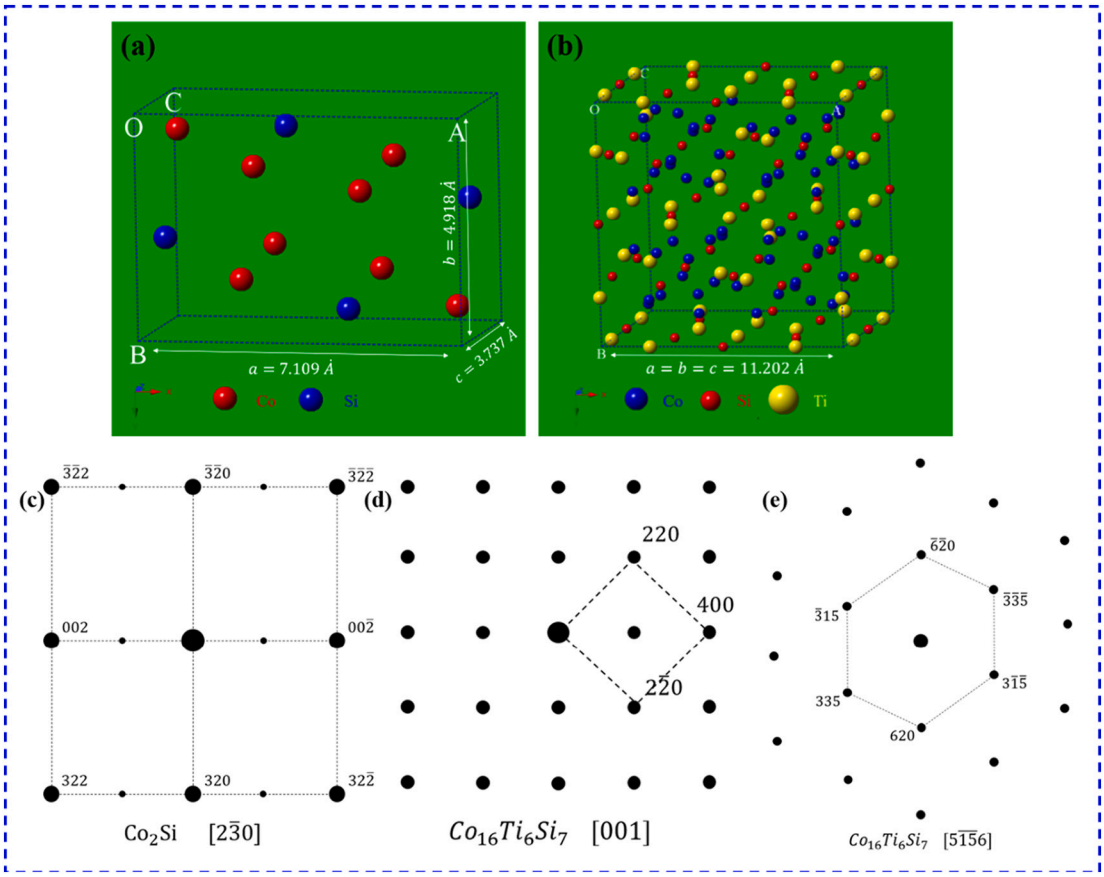

Fig. 6. The generated atomistic structures of Co_2Si (a) and $Co_{16}Ti_6Si_7$ (b) phases, (c) Simulated spots of Co_2Si phase with [2$\bar{3}$0] zone axis, (d) Simulated spots of $Co_{16}Ti_6Si_7$ phase with [001] zone axis, (e) Simulated spots of $Co_{16}Ti_6Si_7$ phase with [5$\bar{1}$56] zone axis.

the matrix. The grain boundaries and elements dissolved in the alloy will distort the matrix, increase the scattering of electrons and reduce the electrical conductivity of the alloy. With the increase of aging temperature and time, alloy elements rapidly precipitate from the supersaturated matrix in the form of precipitates, accompanied by the softening effect of enhanced release of lattice distortion energy during aging, electron scattering decreases and electrical conductivity increases. The softening effect caused by the decrease of dislocation density and release of lattice distortion in the copper matrix and the precipitation of solid solution atoms made the electrical conductivity increase with the increase of aging time and temperature [19,42]. Therefore, the optimum aging parameter of Cu-Co-Si-Ti-Ce alloy was obtained as aging at 500 °C for 60 min.

4.2. Correlation of microstructure and mechanical properties during aging

On the above analysis, the microstructure and the texture of Cu-Co-Si-Ti-Ce alloy underwent substantial changes during the aging process, accompanied by significant changes in performance. As illustrated in Fig. 2(A), the micro-hardness of Cu-Co-Si-Ti-Ce alloy decreased from 225 HV to 208 HV with the aging time from 60 min to 120 min, which can be attributed to the decrease of work hardening [42,43] and the growth of precipitates [4,17]. Fig. 3 shows the EBSD maps of Cu-Co-Si-Ti-Ce alloy aging at 500 °C for 60 min and 120 min, where it can be observed that the appearance of dynamic recrystallization grains, a decrease of texture strength and changes of texture content contributed to the decrease of micro-hardness with the prolong of aging time. In general, the orientation is closely related to deformation, which affects the properties of polycrystalline materials [44]. The initial texture aging at 60 min was characterized by a large volume fraction of Goss, Brass, copper, S texture and a small amount of random orientations. After prolonged aging times to 120 min, a weakening of the texture, i.e. decrease of volume fraction for Goss, Brass, copper, S texture and the texture index, accompanied with a characteristic decrease of the micro-hardness was observed. Therefore, it can be inferred that the high volume fraction of Goss, Brass, copper and S texture was one of the main reasons for the increase of micro-hardness. Furthermore, by the TEM analysis (Fig. 5), it was observed that Co_2Si and $Co_{16}Ti_6Si_7$ phases exhibited coherent and semi-coherent interface relationships with the copper matrix, respectively, which can relieve the interfacial stress and reduce the interface energy [29]. The fine second phases precipitated dispersedly kept the coherent and semi-coherent interface relationships with the copper matrix, resulting in the high strength and medium electrical conductivity of Cu-Co-Si-Ti-Ce alloy.

4.3. Strengthening mechanisms

In the aging process, solution treatment, cold rolling and aging treatment contributed to the Cu-Co-Si-Ti-Ce alloy to obtain high strength. In other words, multiple strengthening mechanisms, mainly including the solid solution strengthening, work-hardening, precipitation strengthening and grain boundary strengthening, contributed to the high strength of Cu-Co-Si-Ti-Ce alloy. To evaluate the specific contributions of mechanisms, the yield strength (σ) of Cu-Co-Si-Ti-Ce alloy can be given by:

$$\sigma = \sigma_{ss} + \sigma_{ds} + \sigma_{p} + \sigma_{GB} \quad (1)$$

Where σ_{ss} represents the stress resulting from solid solution strengthening, σ_{ds} represents the stress resulting from work-hardening strengthening, σ_{p} represents the stress resulting from precipitation

strengthening and σ_{GB} represents the stress resulting from grain boundaries strengthening. And Table S1-S4 gives the parameters used in the yield strength determination where difference strengthening mechanisms were considered.

The degree of solution strengthening can be described as [4]:

$$\sigma_{ss} = G\left(\left|\delta\right| + \frac{1}{20}\right)\left|\eta\right|^{\frac{3}{2}}\sqrt{\frac{x_a}{3}} \quad (2)$$

Where G represents the shear moduli of copper alloy, 46GPa, δ represents the factor of lattice change, 0.1105, η represents the factor for the change of the shear modulus, 0.3171, x_a represents the fraction of solute atoms within the solid solution. In this alloy, the lattice constant of Co is similar to that of copper and is not considered. Moreover, the fraction of Si, Ti and Ce were 0.12%, 0.04% and 0.15%, respectively, which can be obtained from the EDS mapping in Fig. S6. Moreover, the values of the calculation of the dislocation strengthening are listed in Table S1. Therefore, the results of corresponding solution strengthening can be calculated to be 42.4 MPa.

The degree of work-hardening strengthening can be described as [45]:

$$\sigma_{ds} = M\alpha Gb\sqrt{\rho} \quad (3)$$

Where M represents the Taylor factor, 3.06, α represents a geometric constant, 0.3, G represents the shear moduli of copper alloy, 46GPa, b represents the Burgers vector of copper alloy, 0.2556 nm, ρ represents the dislocation density caused by cold deformation, which can be obtained from the KAM map. The values of the calculation of the dislocation strengthening are listed in Table S2. Therefore, the results of corresponding work-hardening strengthening can be calculated to be 170.5 MPa.

Grain boundary strengthening can be described as the Hall-Petch relationship [46,47]:

$$\sigma_{GB} = K_y {d_g}^{-1/2} \quad (4)$$

Where Ky represents the Hall-Petch coefficient, 150 MPa $\mu m^{1/2}$ and dg represents the mean diameter of grain size, 26.8 μm. The values of the calculation of the grain boundary strengthening are listed in Table S3. The results of corresponding grain boundary strengthening can be calculated to be 31.3 MPa.

The precipitation strengthening can be given by the Orowan-Ashby Eq. [24]:

$$\sigma_p = 0.81 \times \frac{MGb}{2\pi(1-\upsilon)^{1/2}} \times \frac{ln(d_p/b)}{(\lambda - d_p)} \quad (5)$$

Where M represents the Taylor factor for the fcc matrix, 3.06, G represents the shear moduli of copper alloy, 46GPa, b represents the Burgers vector of copper alloy, 0.2556 nm, ν represents the Poisson's ratio, 0.34, d_p represents the average size of precipitates, 19.7 nm, λ represents the spacing between particles in the glide plane (100 nm), which can be expressed by $\lambda = \frac{1}{2}d_p\sqrt{\frac{3\pi}{2f_p}}$. f_p represents the volume fraction of the second-phase particles, which can be calculated to be 21.9%. The values of the calculation of the precipitation strengthening are listed in Table S4. Therefore, the results of corresponding precipitation strengthening can be calculated to be 298.6 MPa. Finally, $\sigma = \sigma_{ss} + \sigma_{ds} + \sigma_{GB} + \sigma_p = 42.4 + 170.5 + 31.3 + 298.6 = 542.8\ MPa$, 4.4% error with the actual measured tensile strength of Cu-Co-Si-Ti-Ce alloy (519.5 MPa).

5. Conclusions

In summary, a medium electrical conductivity and excellent mechanical properties of Cu-Co-Si-Ti-Ce alloy was obtained by incorporating the multiple alloy elements, resulting in multiple strengthening during the aging process. The optimum aging parameter of Cu-Co-Si-Ti-Ce alloy was aging at 500 °C for 60 min, accompanied by the excellent aging performance of 225 HV, 702.5 MPa and 40.8% IACS. The volume fraction of Goss, Brass, copper and S texture after 60 min aging process were calculated to be 22.7%, 46.8%, 32.6% and 46%, respectively, higher than that of aging at 120 min, which can be inferred that the high-volume fraction of Goss, Brass, copper and S texture was one of the main reasons for the increase of micro-hardness. Moreover, it was observed that Co_2Si and $Co_{16}Ti_6Si_7$ phases exhibited coherent and semi-coherent interface relationships with the copper matrix, respectively, which can relieve the interfacial stress and reduce the interface energy. Finally, the contributions of solid solution strengthening, work-hardening, grain boundary strengthening and precipitation strengthening were calculated, contributing most to the precipitation strengthening.

Declaration of Competing Interest

The authors declare that they have no known competing financial interests or personal relationships that could have appeared to influence the work reported in this paper.

Meng Zhou, Yongfeng Geng, Yi Zhang, Haoyan Hu, Yijie Ban, Xu Li, Yanlin Jia, Baohong Tian, Yong Liu, Alex A. Volinsky.

Data availability

No data was used for the research described in the article.

Acknowledgments

This work was supported by the National Natural Science Foundation of China (52071134), Outstanding Talents Innovation Fund of Henan Province (ZYQR201912164), the Program for Innovative Research Team at the University of the Henan Province (22IRTSTHN001), China Postdoctoral Science Foundation (2020M682316,2021T140779) and Special Research and Development Project of Henan Academy of Sciences (220910009). AV acknowledges support from the Government of the Russian Federation No. 220 of 09 April 2010 (Agreement No. 075-15-2021-612 of 04 June 2021).

Appendix A. Supplementary data

Supplementary data to this article can be found online at https://doi.org/10.1016/j.matchar.2022.112494.

References

[1] Y.F. Geng, Y.J. Ban, B.J. Wang, X. Li, K.X. Song, Y. Zhang, Y.L. Jia, B.H. Tian, Y. Liu, A.A. Volinsky, A review of microstructure and texture evolution with nanoscale precipitates for copper alloys, J. Mater. Res. Technol. 9 (5) (2020) 11918–11934.
[2] K.X. Song, Y.F. Geng, Y.J. Ban, Y. Zhang, Z. Li, X.J. Mi, J. Cao, Y.J. Zhou, X. B. Zhang, Effects of strain rates on dynamic deformation behavior of Cu-20Ag alloy, J. Mater. Sci. Technol. 79 (2021) 75–87.
[3] D. Zhao, Q.M. Dong, P. Liu, B.X. Kang, J.L. Huang, Z.H. Jin, Aging behavior of Cu-Ni-Si alloy, Mater. Sci. Eng. A 361 (1–2) (2003) 93–99.
[4] Q. Lei, Z. Xiao, W. Hu, B. Derby, Z. Li, Phase transformation behaviors and properties of a high strength Cu-Ni-Si alloy, Mater. Sci. Eng. A 697 (2017) 37–47.
[5] Z. Zhao, Y. Zhang, B.H. Tian, Y.L. Jia, Y. Liu, K.X. Song, A.A. Volinsky, Co effects on Cu-Ni-Si alloys microstructure and physical properties, J. Alloys Compd. 797 (2019) 1327–1337.
[6] H. Azzeddine, B. Mehdi, L. Hennet, D. Thiaudiere, B. Alili, M. Kawasaki, D. Bradai, T.G. Langdon, An in situ synchrotron X-ray diffraction study of precipitation kinetics in a severely deformed Cu-Ni-Si alloy, Mater. Sci. Eng. A 597 (2014) 288–294.
[7] S. Lee, H. Matsunaga, X. Sauvage, Z. Horita, Strengthening of Cu-Ni-Si alloy using high-pressure torsion and aging, Mater. Charact. 90 (2014) 62–70.
[8] N. Wang, Y.D. Shen, Q. An, K.M. Reddy, M.J. Jin, R. Karre, X.D. Wang, Microstructure evolution and mechanical property of Cu-15Ni-8Sn-0.2Nb alloy during aging treatment, J. Mater. Sci. Technol. 86 (2021) 227–236.
[9] J.C. Zhao, M.R. Notis, Spinodal decomposition, ordering transformation, and discontinuous precipitation in a Cu-15Ni-8Sn alloy, Acta Mater. 46 (12) (1998) 4203–4218.

[10] B.J. Wang, Y. Zhang, B.H. Tian, Y.L. Jia, Alex A. Volinsky, V. Yakubovd, Y. Liu, K. X. Song, M. Fu, Nanoscale precipitates evolution and strengthening mechanism of the aged Cu-Mg-Fe-Sn-P-Y electrical contact wire, J. Mater. Res. Technol. 9 (3) (2020) 6352–6359.
[11] W.Y. Wang, J.L. Zhu, N.N. Qin, Y.F. Zhang, S.Y. Li, Z. Xiao, Q. Lei, Z. Li, Effects of minor rare earths on the microstructure and properties of Cu-Cr-Zr alloy, J. Alloys Compd. 847 (2020), 155762.
[12] K. Abib, J.A.M. Balanos, B. Alili, D. Bradai, On the microstructure and texture of Cu-Cr-Zr alloy after severe plastic deformation by ECAP, Mater. Charact. 112 (2015) 252–258.
[13] X. Wang, Z. Xiao, W.T. Qiu, Z. Li, F. Liu, The evolution of microstructure and properties of a Cu-Ti-Cr-Mg-Si alloy with high strength during the multi-stage thermomechanical treatment, Mater. Sci. Eng. A 803 (2021), 140510.
[14] C. Li, X.H. Wang, B. Li, J. Shi, Y.F. Liu, P. Xiao, Effect of cold rolling and aging treatment on the microstructure and properties of Cu3Ti2Mg alloy, J. Alloys Compd. 818 (2020), 152915.
[15] H. Tsubakino, R. Nozato, A. Yamamoto, Precipitation sequence for simultaneous continuous and discontinuous modes in Cu-Be binary alloys, Mater. Sci. Technol. 9 (4) (1993) 288–294.
[16] Y.C. Cao, S.Z. Han, E.A. Choi, J.H. Ahn, X.J. Mi, S.J. Lee, H. Shin, S.S. Kim, J. Lee, Effect of inclusion on strength and conductivity of Cu-Ni-Si alloys with discontinuous precipitation, J. Alloys Compd. 843 (2020), 156006.
[17] Q. Lei, S.Y. Li, J.L. Zhu, Z. Xiao, F.F. Zhang, Z. Li, Microstructural evolution, phase transition, and physics properties of a high strength Cu-Ni-Si-Al alloy, Mater. Charact. 147 (2019) 315–323.
[18] Q. Lei, Z. Li, Y. Gao, X. Peng, B. Derby, Microstructure and mechanical properties of a high strength Cu-Ni-Si alloy treated by combined aging processes, J. Alloys Compd. 695 (2017) 2413–2423.
[19] J. Li, G.J. Huang, X.J. Mi, L.J. Peng, H.F. Xie, Y.L. Kang, Microstructure evolution and properties of a quaternary Cu-Ni-Co-Si alloy with high strength and conductivity, Mater. Sci. Eng. A 766 (2019), 138390.
[20] W. Wang, H.J. Kang, Z.N. Chen, Z.J. Chen, C.L. Zou, R.G. Li, Effects of Cr and Zr additions on microstructure and properties of Cu-Ni-Si alloys, Mater. Sci. Eng. A 673 (2016) 378–390.
[21] Y.J. Ban, Y. Zhang, Y.L. Jia, B.H. Tian, A.A. Volinsky, X.H. Zhang, Q.F. Zhang, Y. F. Geng, Y. Liu, Xu Li, Effects of Cr addition on the constitutive equation and precipitated phXu Li, ases of copper alloy during hot deformation, Mater. Des. 191 (2020), 108613.
[22] Q. Lei, Z. Li, C. Dai, J. Wang, X. Chen, J.M. Xie, W.W. Yang, D.L. Chen, Effect of aluminum on microstructure and property of Cu-Ni-Si alloys, Mater. Sci. Eng. A 572 (2013) 65–74.
[23] Q. Lei, Z. Li, M.P. Wang, L. Zhang, Z. Xiao, Y.L. Jia, The evolution of microstructure in Cu-8.0Ni-1.8Si-0.15Mg alloy during aging, Mater. Sci. Eng. A 527 (2010) 6728–6733.
[24] Z.L. Zhao, Z. Xiao, Z. Li, W.T. Qiu, H.Y. Jiang, Q. Lei, Z.R. Liu, Y.B. Jiang, S. J. Zhang, Microstructure and properties of a Cu-Ni-Si-Co-Cr alloy with high strength and high conductivity, Mater. Sci. Eng. A 759 (2019) 396–403.
[25] J.Y. Cheng, B.B. Tang, F.X. Yu, B. Shen, Evaluation of nanoscale precipitates in a Cu-Ni-Si-Cr alloy during aging, J. Alloys Compd. 614 (2014) 189–195.
[26] Y.F. Geng, X. Li, H.L. Zhou, Y. Zhang, Y.L. Jia, B.H. Tian, Y. Liu, A.A. Volinsky, X. H. Zhang, K.X. Song, G.X. Wang, L.H. Li, J.R. Hou, Effect of Ti addition on microstructure evolution and precipitation in Cu-Co-Si alloy during hot deformation, J. Alloys Compd. 821 (2020), 153518.
[27] Y.F. Geng, Y. Zhang, K.X. Song, Y.L. Jia, X. Li, H.R. Stock, H.L. Zhou, B.H. Tian, Y. Liu, A.A. Volinsky, X.H. Zhang, P. Liu, X.H. Chen, Effect of Ce addition on microstructure evolution and precipitation in Cu-Co-Si-Ti alloy during hot deformation, J. Alloys Compd. 842 (2020), 155666.
[28] Y.K. Wu, Y. Li, J.Y. Lu, S. Tan, F. Jiang, J. Sun, Correlations between microstructures and properties of Cu-Ni-Si-Cr alloy, Mater. Sci. Eng. A 731 (2018) 403–412.
[29] J. Yi, Y.L. Jia, Y.Y. Zhao, Z. Xiao, K.J. He, Q. Wang, M.P. Wang, Z. Li, Precipitation behavior of Cu-3.0Ni-0.72Si alloy, Acta Mater. 166 (2019) 261–270.
[30] Y.K. Xie, Y.L. Deng, Y. Wang, X.B. Guo, Effect of asymmetric rolling and subsequent ageing on the microstructure, texture and mechanical properties of the Al-Cu-Li alloy, J. Alloys Compd. 836 (2020), 155445.
[31] S.L. Fu, P. Liu, X.H. Chen, H.L. Zhou, F.C. Ma, W. Li, K. Zhang, Effect of aging process on the microstructure and properties of Cu-Cr-Ti alloy, Mater. Sci. Eng. A 802 (2021), 140598.
[32] J.Z. Huang, Z. Xiao, J. Dai, Z. Li, H.Y. Jiang, W. Wang, X.X. Zhang, Microstructure and properties of a novel Cu-Ni-Co-Si-Mg alloy with super-high strength and conductivity, Mater. Sci. Eng. A 744 (2019) 754–763.
[33] F. Liu, J. Li, L.J. Peng, G.J. Huang, H.F. Xie, J.M. Ma, X.J. Mi, Simultaneously enhanced hardness and electrical conductivity in a Cu-Ni-Si alloy by addition of cobalt, J. Alloys Compd. 862 (2021), 158667.
[34] S.L. Fu, P. Liu, X.H. Chen, H.L. Zhou, F.C. Ma, W. Li, K. Zhang, Effect of aging process on the microstructure and properties of Cu-Cr-Ti alloy, Mater. Sci. Eng. A 802 (2021), 140598.
[35] J. Liu, X.H. Wang, J. Chen, J.T. Liu, The effect of cold rolling on age hardening of Cu-3Ti-3Ni-0.5Si alloy, J. Alloys Compd. 797 (2019) 370–379.
[36] C. Li, X.H. Wang, B. Li, J. Shi, Y.F. Liu, P. Xiao, Effect of cold rolling and aging treatment on the microstructure and properties of Cu-3Ti-2Mg alloy, J. Alloys Compd. 818 (2020), 152915.
[37] Z.K. Guo, J.C. Jie, J.M. Liu, S.P. Yue, S.C. Liu, T.J. Li, Effect of cold rolling on aging precipitation behavior and mechanical properties of Cu-15Ni-8Sn alloy, J. Alloys Compd. 848 (2020), 156275.
[38] Y.S. Wu, X.Z. Qin, C.S. Wang, L.Z. Zhou, Influence of phosphorus on hot deformation microstructure of a Ni-Fe-Cr based alloy, Mater. Sci. Eng. A 768 (2019), 138454.
[39] Y.S. Wu, Z. Liu, X.Z. Qin, C.S. Wang, L.Z. Zhou, Effect of initial state on hot deformation and dynamic recrystallization of Ni-Fe based alloy GH984G for steam boiler applications, J. Alloys Compd. 795 (2019) 370–384.
[40] Y.F. Chen, B. Yang, Y.T. Zhou, Y. Wu, H.H. Zhu, Evaluation of pitting corrosion in duplex stainless steel Fe20Cr9Ni for nuclear power application, Acta Mater. 197 (2020) 172–183.
[41] H.Y. Yang, K.Q. Li, Y.Q. Bu, J.M. Wu, Y.T. Fang, L. Meng, J.B. Liu, H.T. Wang, Nanoprecipitates induced dislocation pinning and multiplication strategy for designing high strength, plasticity and conductivity Cu alloys, Scr. Mater. 195 (2021), 113741.
[42] S. Semboshi, S. Sato, A. Iwase, T. Takasugi, Discontinuous precipitates in age-hardening CuNiSi alloys, Mater. Charact. 115 (2016) 39–45.
[43] J. Chalon, J.D. Guérin, L. Dubar, A. Dubois, Puchi-Cabrera, Characterization of the hot-working behavior of a Cu-Ni-Si alloy, Mater. Sci. Eng. A 667 (2016) 77–86.
[44] J. Liu, X.H. Wang, J. Chen, J.T. Liu, The effect of cold rolling on age hardening of Cu-3Ti-3Ni-0.5Si alloy, J. Alloys Compd. 797 (2019) 370–379.
[45] Z.W. Wang, W.J. Lu, H. Zhao, C.H. Liebscher, J.Y. He, D. Ponge, D. Raabe, Z.M. Li, Ultrastrong lightweight compositionally complex steels via dual-nanoprecipitation, Sci. Adv. 6 (2020) 1–7.
[46] Y. Zhang, N.R. Tao, K. Lu, Mechanical properties and rolling behaviors of nanograined copper with embedded nano-twin bundles, Acta Mater. 56 (2008) 2429–2440.
[47] N. Hansen, Hall-Petch relation and boundary strengthening, Scr. Mater. 51 (2004) 801–806.